Supporting Information

A Bimodal MRI-traceable Nanozyme with Immune-Activated Capability for Immunotherapy of Lung Metastases

Qiuyi Xu [a,b,#], *Sha Li* [a,b,#], *Maosong Qiu* [a,b], *Xiaoxun Liu* [a,b], *Meiju Sui* [a,b], *Lei Zhang* [a,b], *Xin Zhou* [a,b,c] *and Shizhen Chen* [a,b,c*]

[a] State Key Laboratory of Magnetic Resonance Spectroscopy and Imaging, National Center for Magnetic Resonance in Wuhan, Wuhan Institute of Physics and Mathematics, Innovation Academy for Precision Measurement Science and Technology, Chinese Academy of Sciences, Wuhan 430071, P. R. China.

[b] University of Chinese Academy of Sciences, Beijing 100049, P. R. China.

[c] School of Biomedical Engineering, Hainan University, Sanya 572019, P. R. China.

[*] Corresponding author: chenshizhen@wipm.ac.cn.

[#] These authors contributed equally to this work.

1. Supplementary Experimental Section

Materials

Except where otherwise noted, all chemicals were used without further purification. Hexadecyl trimethyl ammonium bromide (CTAB), sodium hydroxide (NaOH), ethanol, and H_2O_2 were obtained from Shanghai Hushi Chemical Co., Ltd. 1-Bromoheptadecafluorooctane (PFOB), tetraethyl orthosilicate (TEOS), and 3,3',5,5'-tetramethylbenzidine (TMB) were acquired from Aladdin (Shanghai, China). 4-Morpholineethanesulfonic acid (MES) was purchased from Adamas-beta (Shanghai, China). 5,5'-Dithiobis (2-nitrobenzoic acid) (DTNB) and indocyanine green (ICG) were obtained from Bide Pharmatech Ltd (Shanghai, China). 5,5-dimethyl-1-pyrroline N-oxide (DMPO), 5-tert-butoxycarbonyl-5-methyl-1-pyrroline-N-oxide (BMPO), and SOD Assay Kit-WST were obtained from DOJINDO (Japan). 4',6-diamidino-2-phenylindole (DAPI), Calcein/PI cell viability/cytotoxicity Assay Kit, and Annexin V-FITC/PI Apoptosis Kit were obtained from Beyotime Biotechnology. 2',7'-dichlorodihydrofluorescein diacetate (DCFH-DA) and Mitochondrial Membrane Potential Assay Kit with JC-1 were purchased from Solarbio (Beijing, China). Antibodies against F4/80, CD86, and CD206 for flow cytometry were purchased from Thermo Fisher (Waltham, USA). Anti-HMGB1 antibody (ab79823) and anti-calreticulin (CRT) antibody (ab92516) were obtained from Abcam (Cambridge, UK). STING Rabbit antibody (A21051), IRF3 Rabbit antibody (A19717), Phospho-IRF3-S396 Rabbit antibody (AP0623), Phospho-TBK1 Rabbit antibody (AP1418), IFN-beta Rabbit antibody (A22740), and FITC Goat Anti-Rabbit lgG(H+L) (AS011) were obtained from ABclonal Technology Co., Ltd (Wuhan, China). Mouse Tumor Necrosis Factor Alpha (TNF-α) ELISA Kit and Mouse Interferon Gamma (IFN-γ) ELISA Kit were obtained from Jianglai biology (Shanghai, China).

Characterization

The morphology of nanoparticles were tested by the TEM (FEI Company, USA). The elemental distribution of FMBI NPs was tested by the HAADF-STEM (Oxford x-met

8000). Dynamic light scattering (DLS) and zeta potential measurements were conducted using a ZS nanohybrid analyzer (Malvern, England). Ultraviolet-visible-near infrared (UV-vis-NIR) absorption spectra of different samples were recorded by an Evolution 220 UV-vis spectrophotometer (Thermo Fisher Scientific Inc., USA). The valence states of Mn in the nanoparticles were analyzed using X-ray photoelectron spectroscopy (ESCA Lab 250, Thermo Fisher Scientific, USA). The Mn concentration of the samples was measured by ICP-OES (Agilent 5110, USA) or ICP-MS (PQ-MS, Germany). The surface area and pore diameter distribution were obtained on the nitrogen adsorption apparatus (ASAP 2420, Micromeritics, USA). The Electron spin resonance (ESR) spectra were acquired using a spectrometer (JES-FA200, JEOL, Japan) at room temperature. All *in vitro and in vivo* ^{1}H T_1-weighted MRI and ^{19}F MRI experiments were performed on a 9.4 T micro-imaging system (Bruker Avance 400, Ettlingen, Germany).

Statistical Analysis

Differences between experimental groups and control samples were assessed by Student's t-test using GraphPad Prism 8 Software. n.s. was not significant, *$p < 0.05$ was considered as a significant difference; **$p < 0.01$ and ***$p < 0.001$ were considered as highly and very significant.

2. Supplementary Figures

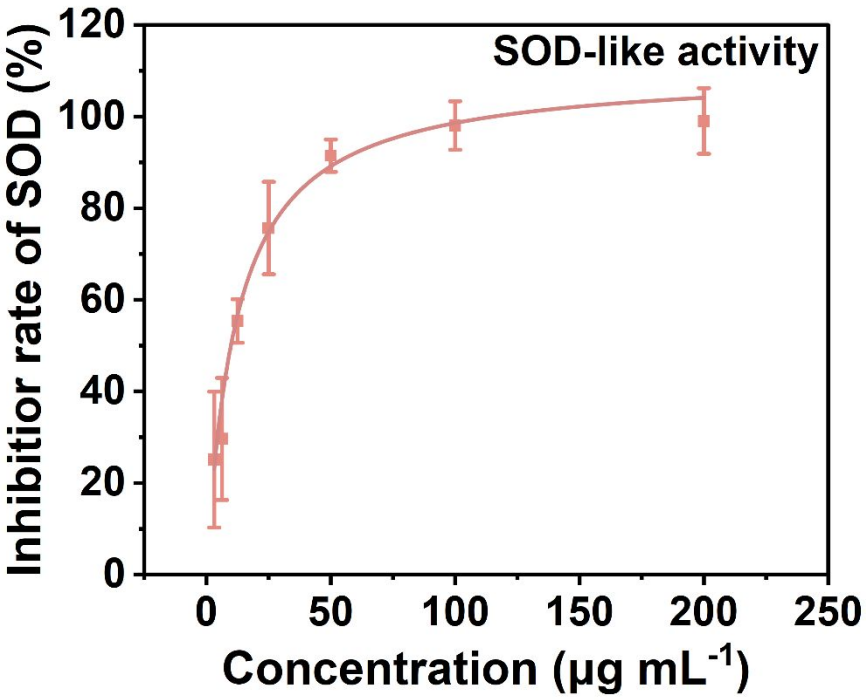

Figure S1. The SOD-like activity curve of FMBI NPs.

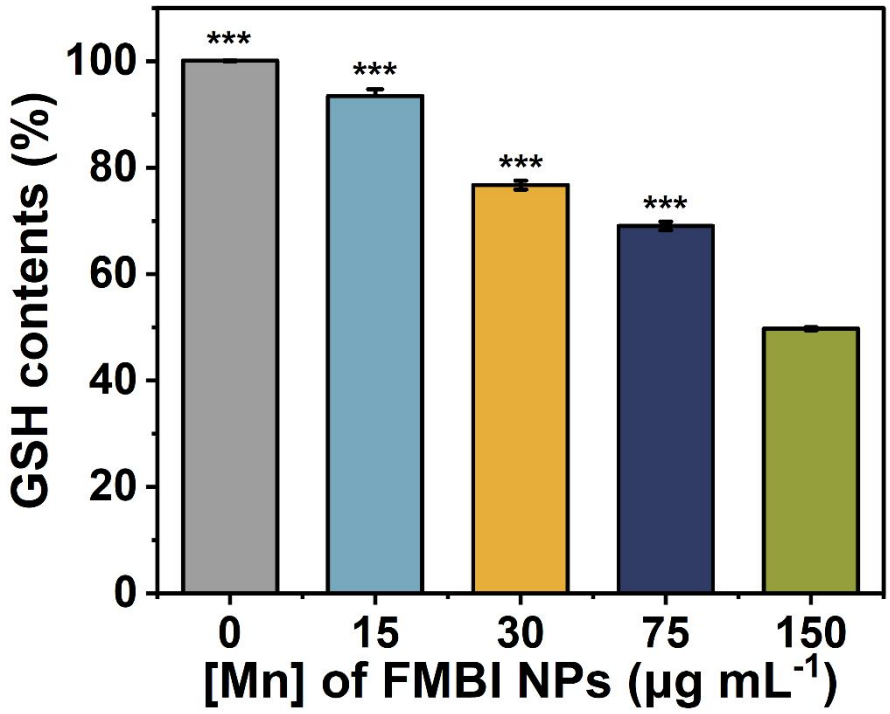

Figure S2. GSH consumption rate at various FMBI NP concentrations.

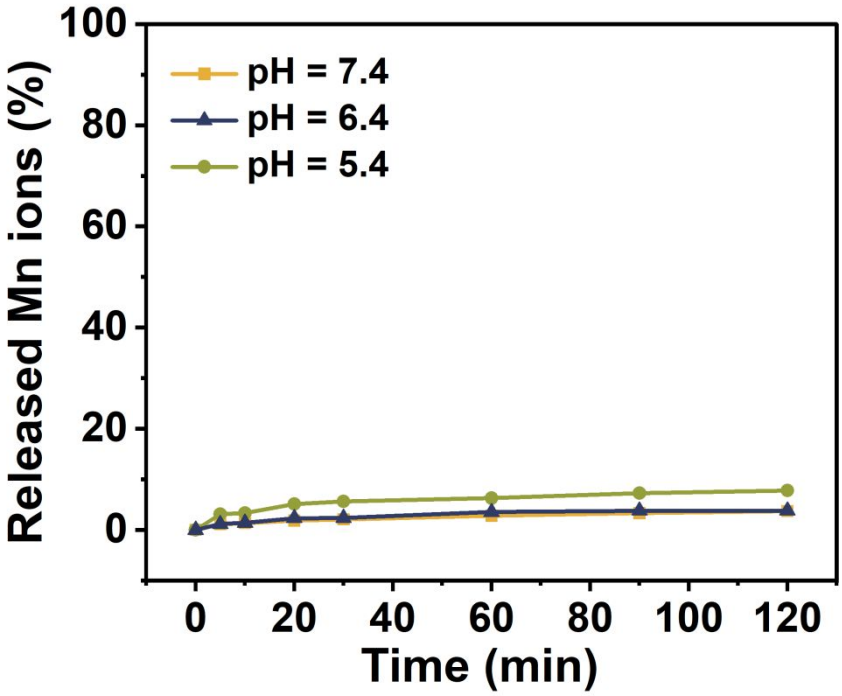

Figure S3. Accumulated release profiles of Mn ions under different pH values.

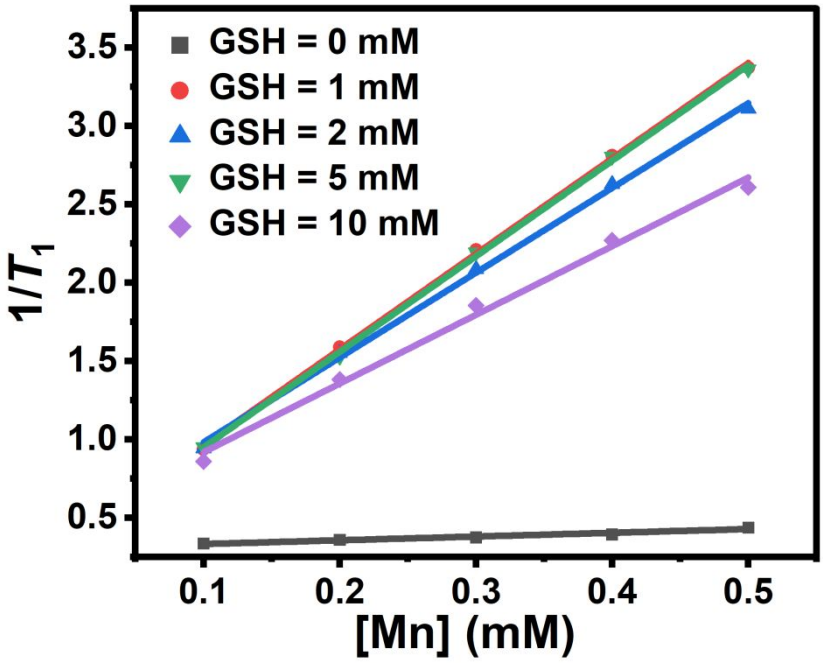

Figure S4. The longitudinal relaxivity of FMBI NPs treated with different concentrations of GSH.

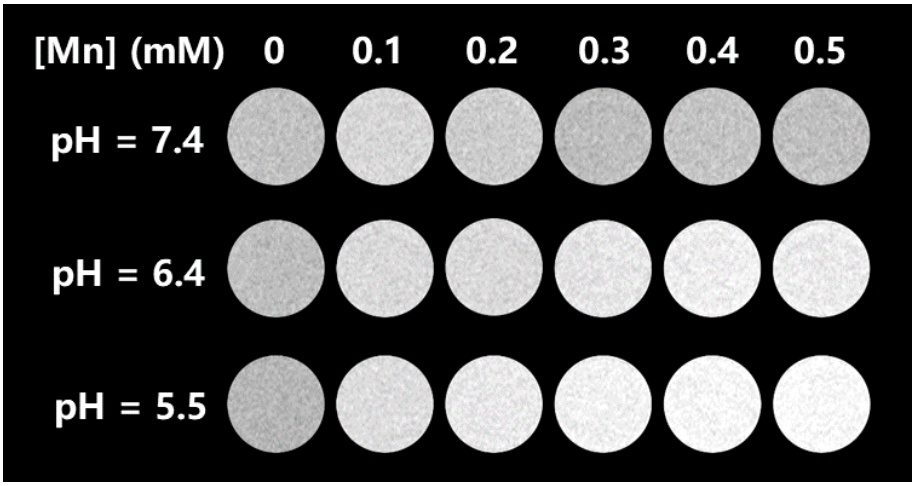

Figure S5. ^{1}H T_1-weighted MRI of FMBI NPs at different concentrations and pH values (7.4, 6.4, 5.5).

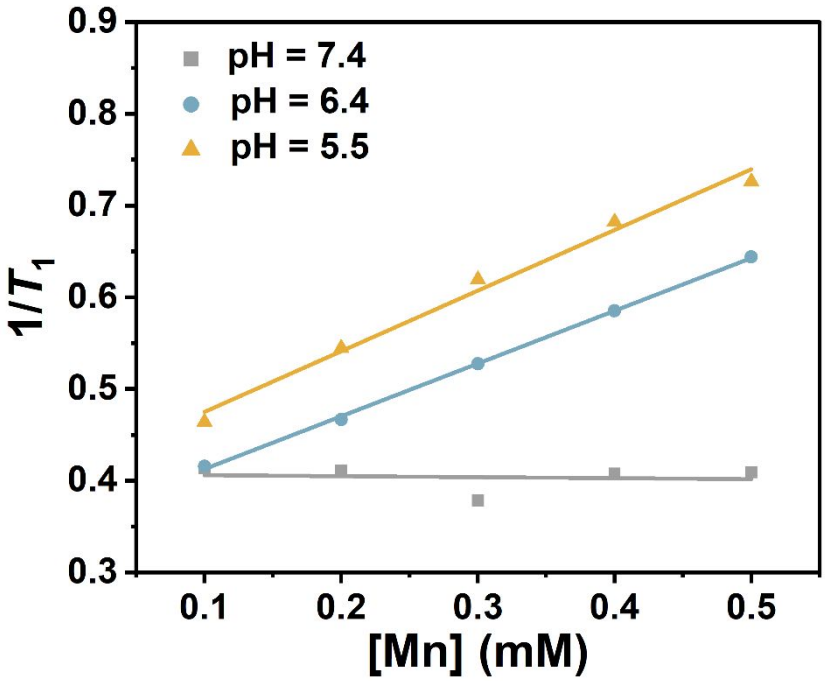

Figure S6. The longitudinal relaxivity of FMBI NPs under different pH values.

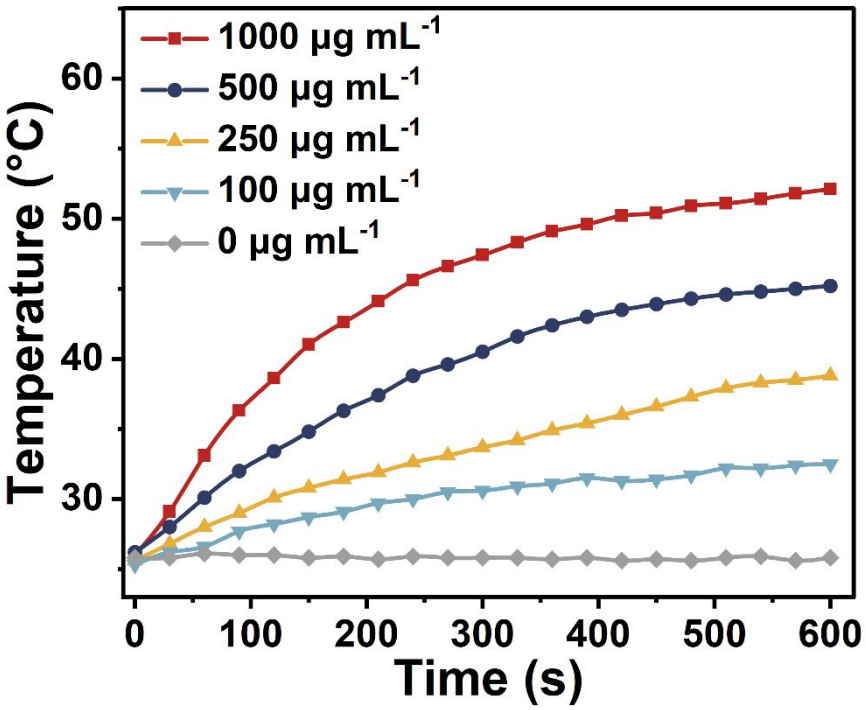

Figure S7. Time-temperature curves of FMBI NPs aqueous solutions at various concentrations (0, 100, 250, 500, and 1000 μg mL^{-1}) under 808 nm laser irradiation (, 0.5 W cm^{-2}, 10 min) .

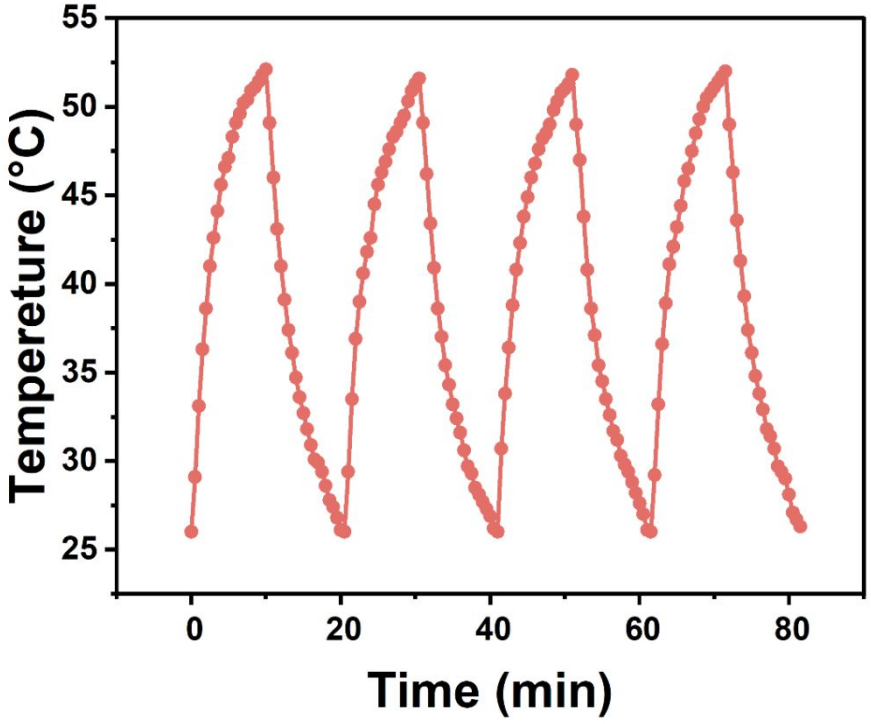

Figure S8. Temperature variation curves of FMBI NPs aqueous solution over four on /off cycles under the 808 nm laser irradiation (10 min irradiation, 10 min cooling).

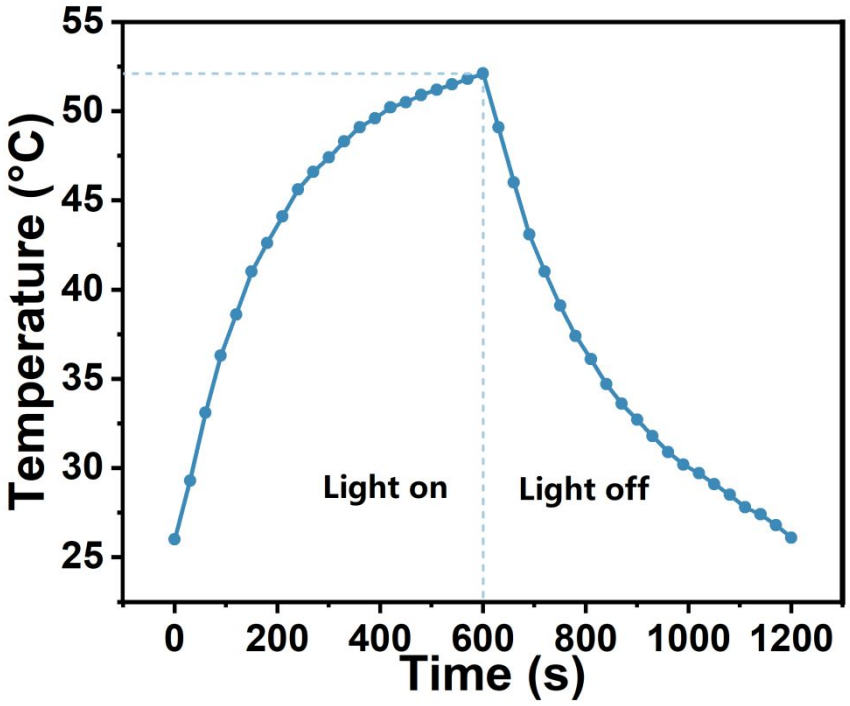

Figure S9. The photothermal effect of FMBI NPs aqueous solution (1000 μg mL^{-1}) irradiated with an 808 nm laser (1.0 W cm^2).

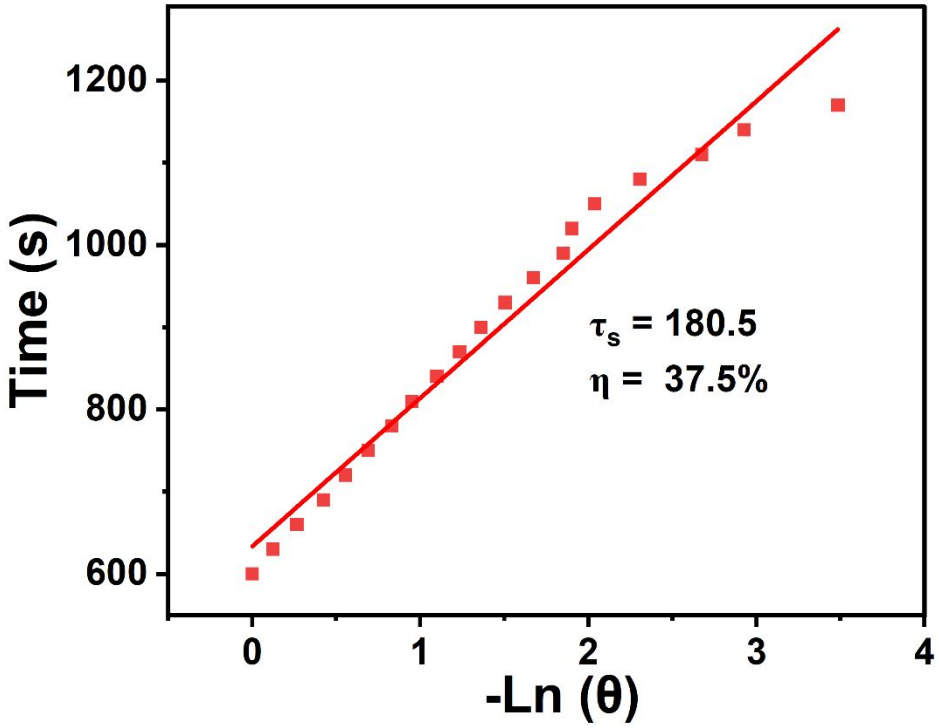

Figure S10. Calculation of the photothermal conversion efficiency (η) of FMBI NPs at 808 nm. The photothermal effect of an FMBI NPs aqueous dispersion was assessed under 808 nm laser irradiation for 10 min, followed by laser deactivation.

Photothermal Conversion Efficiency Evaluation. An 808 nm near-infrared laser (Beijing Leizhiwei Optoelectronic Technology Co., Ltd.) was used to irradiate different solutions. The laser power was 1.0 W cm^{-2}, and the temperature change was detected and recorded in real time using a near-infrared thermal imager. The photothermal conversion efficiency (η) of FMBI NPs was calculated using the following equations.[1]

$$\eta = \frac{hS(T_{max} - T_{surr}) - Q_{dis}}{I(1 - 10^{-A_{808}})} \times 100\% \quad \text{(S1)}$$

Where h is the heat transfer coefficient of the nanocomposites; S is the area cross section of irradiation; T_{max} is the equilibrium temperature; T_{surr} is ambient temperature of the surroundings; Q_{dis} is the baseline energy input from the light absorption by the solvent; I is the laser power density (1.0 W cm^{-2}); $A_{808\ nm}$ is the absorbance of the FMBI NPs (1000 μg mL^{-1}) at wavelength of 808 nm. Because the value of hS remains unknown, a dimensionless driving force temperature (θ) is introduced to calculate the

value of hS using the following equations:

$$\theta = \frac{T - T_{surr}}{T_{max} - T_{surr}} \quad \text{(S2)}$$

$$t = -\tau s \ln \theta \quad \text{(S3)}$$

$$\tau_s = \frac{\sum m_i C_{p,i}}{hS} \quad \text{(S4)}$$

At the cooling stage of the aqueous dispersion, t is cooling time after irradiation, and the time constant (τ_s) for heat transfer from the system could be determined as τ_s = 180.5 s by applying the linear time data from the cooling period versus the negative natural logarithm of driving force temperature. Where m_i and $C_{p,i}$ are the mass (0.5 g) and the thermal capacity (4.2 $J \cdot g^{-1} \cdot °C^{-1}$) of deionized water used as a solvent, respectively. In addition, Q_{dis} was measured independently to be 0.54 mW, the (T_{max}-T_{Surr}) was 26.1 °C, I was 1.0 W cm^{-2}, A_{808} was the absorbance (0.718) of FMBI NPs (1000 μg mL^{-1}) at 808 nm. Based on the above equations, the value of hS is deduced to be 11.6 Mw $°C^{-1}$. Finally, the 808 nm laser photothermal conversion efficiency (η) of FMBI NPs can be calculated to be 37.5%.

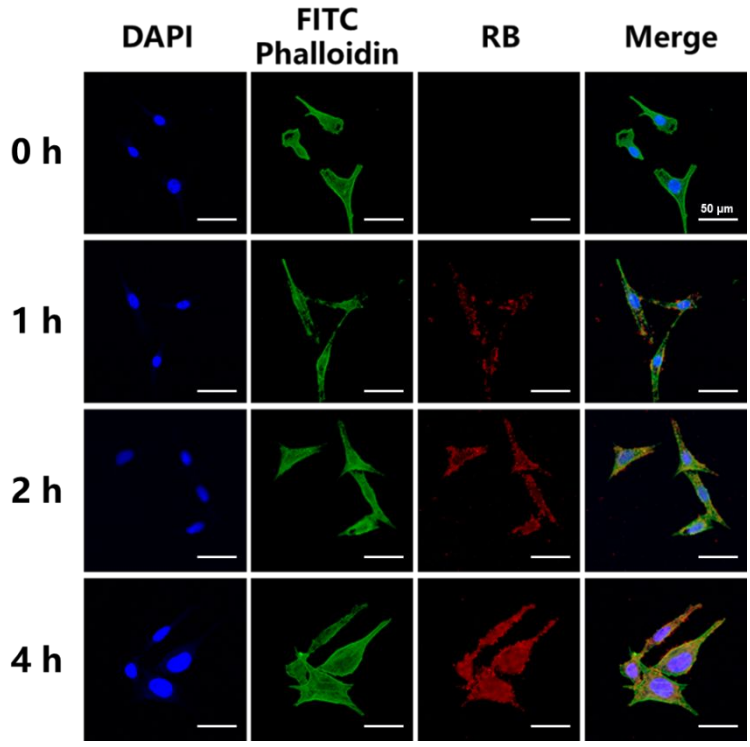

Figure S11. Cellular uptake of B16F10 cells after incubation with Rhodamine B-labeled FMBI NPs (40 μg mL^{-1}).

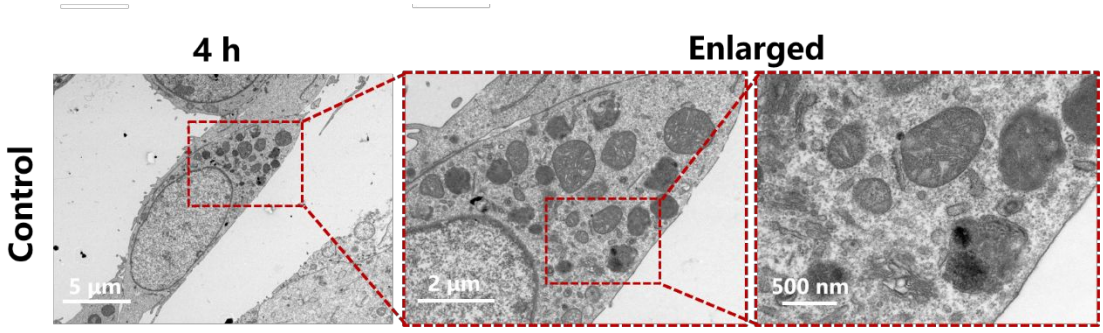

Figure S12. Bio-TEM images of B16F10 cells incubated with PBS (control) for 4 h.

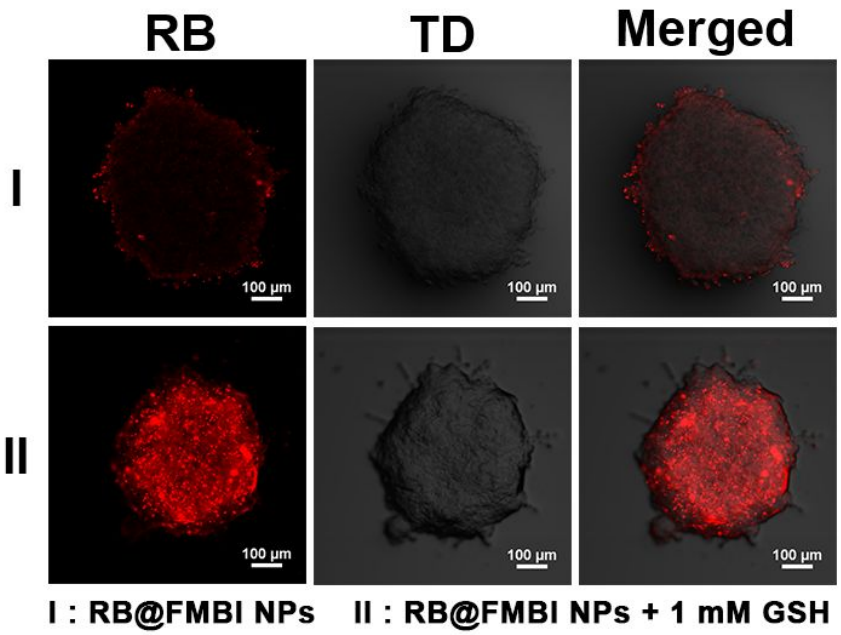

Figure S13. The tumor penetration images of A549 cell-based multicellular spheroids after incubation with RB@FMBI NPs and RB@FMBI NPs plus 1 mM GSH for 3 h.

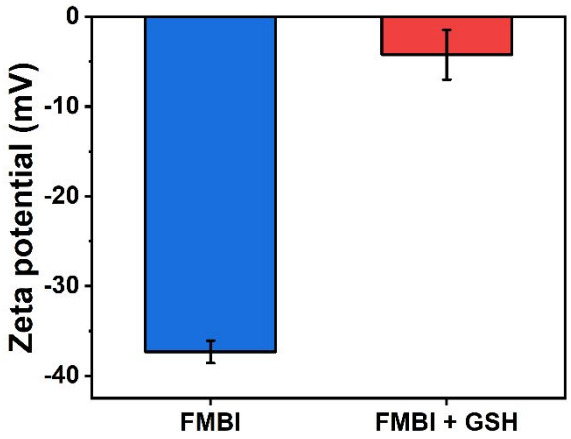

Figure S14. Zeta potential of FMBI NPs and FMBI NPs plus 1 mM GSH.

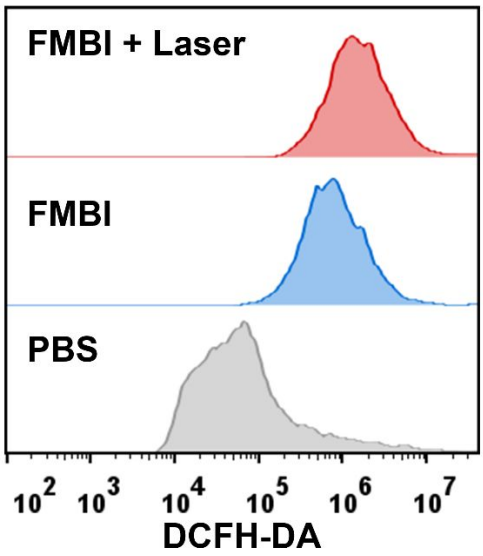

Figure S15. The flow cytometry analysis of ROS levels in B16F10 cells after different treatments.

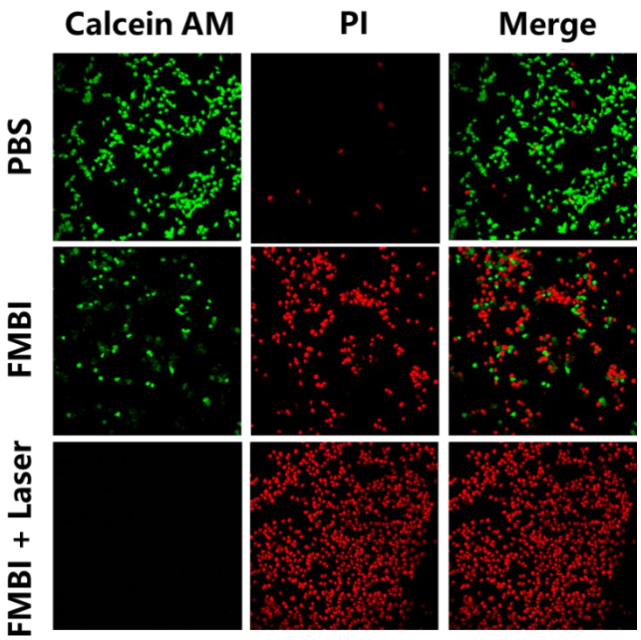

Figure S16. CLSM images of B16F10 cells with different treatments. All the cells were dyed with Calcein AM/PI.

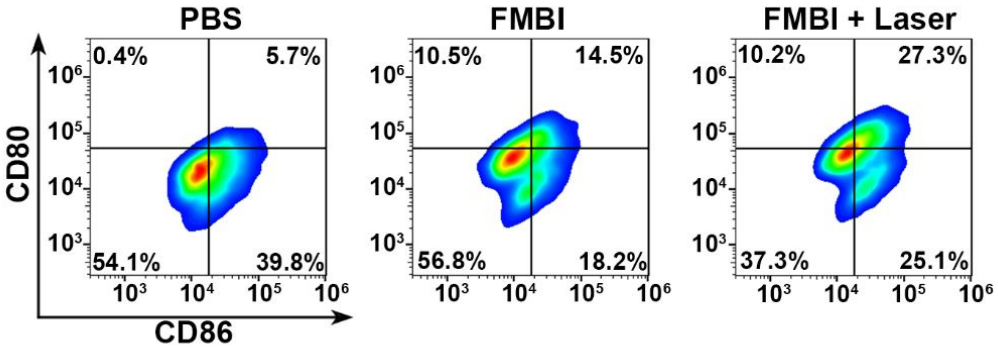

Figure S17. Representative flow diagram of FMBI NPs activating maturation of DCs.

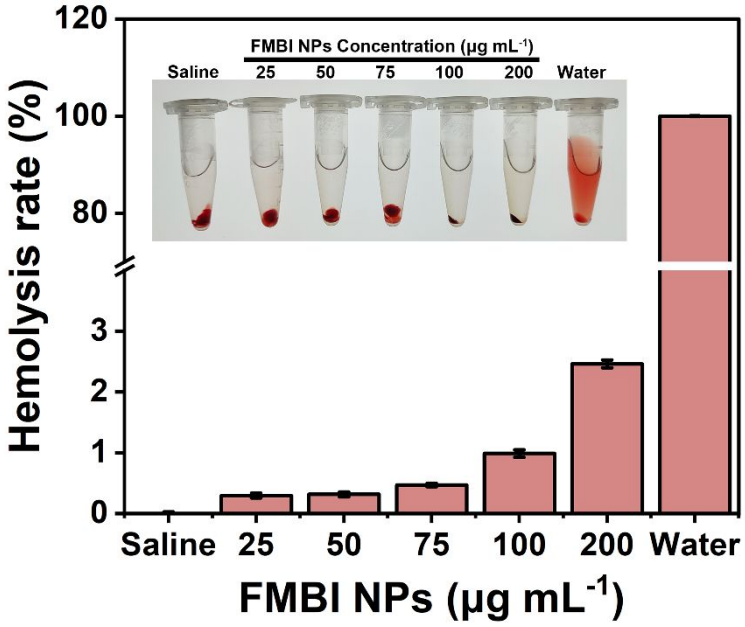

Figure S18. Hemolysis of RBCs treated with different concentrations of FMBI NPs (means ± SD, n = 3).

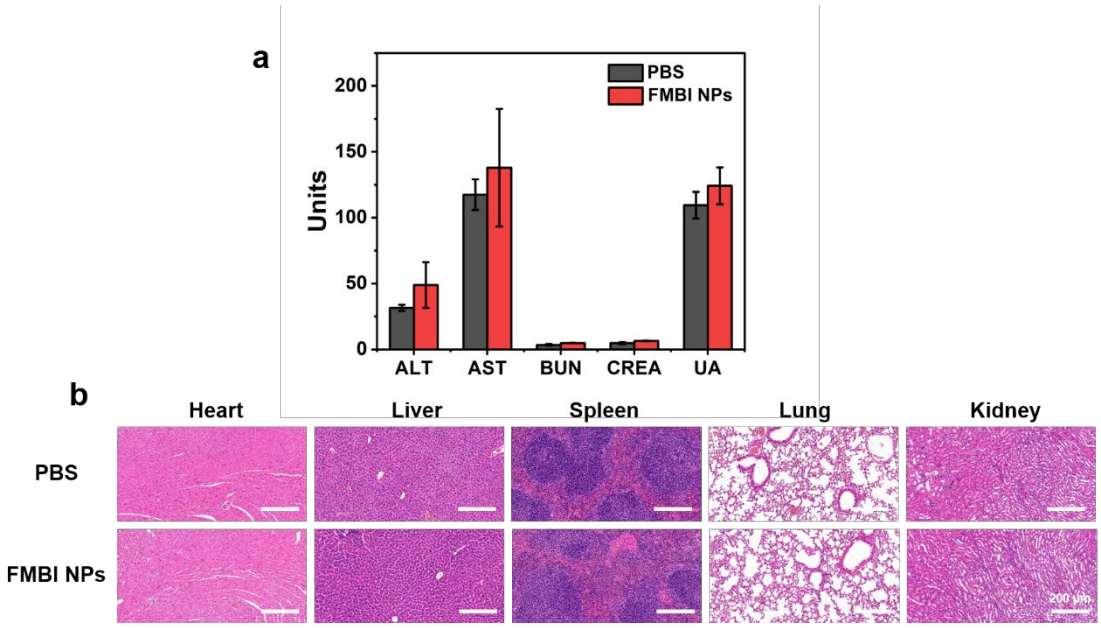

Figure S19. *In vivo* biocompatibility evaluation of FMBI NPs 7 days after *i.v.* administration. (a) Blood biochemical analysis (mean ± S.D., n = 3). (b) Histological analysis of mouse heart, liver, spleen, lungs, and kidneys following *i.v.* administration of PBS or FMBI NPs.

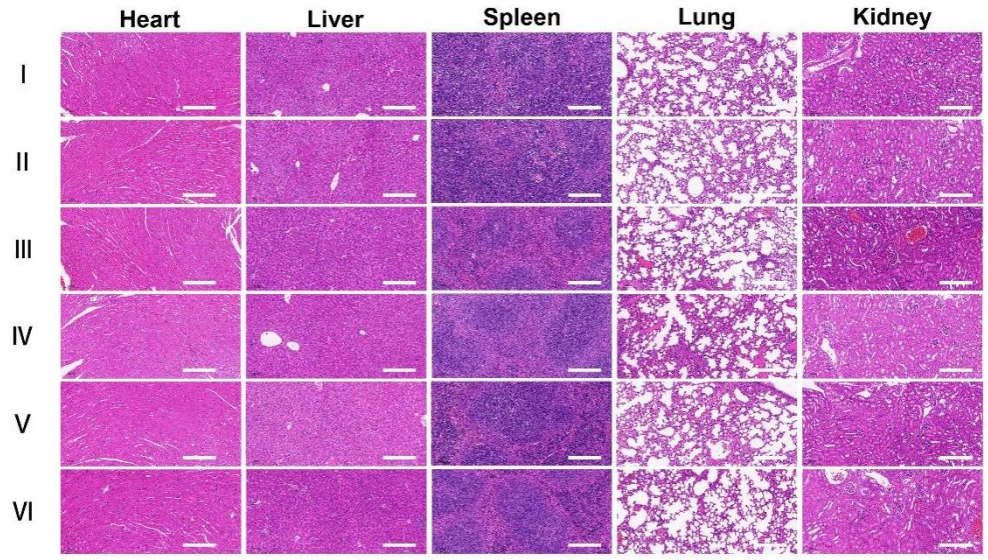

Figure S20. H&E stained tissue sections collected from mice after various treatments. (Group Ⅰ: PBS, Ⅱ: PBS + Laser, Ⅲ: FMB NPs, Ⅳ: FMB NPs + Laser, Ⅴ: FMBI NPs, Ⅵ: FMBI NPs + Laser, scale bar = 200 μm.)

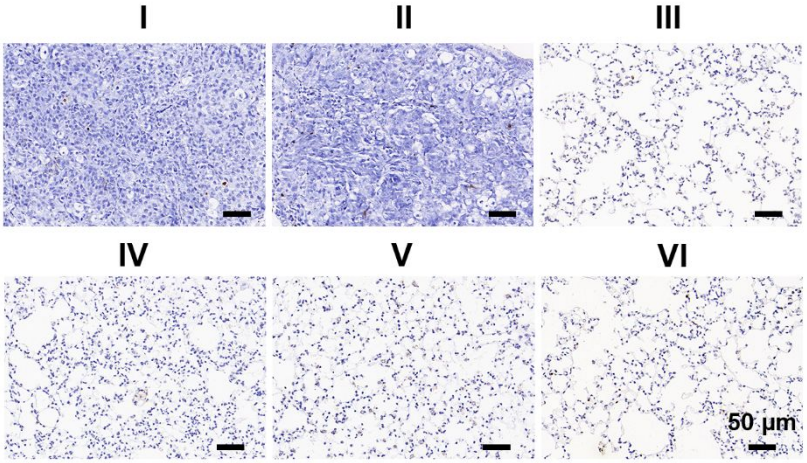

Figure S21. TUNEL-stained lung tissue sections collected from mice after various treatments. (Group Ⅰ: PBS, Ⅱ: PBS + Laser, Ⅲ: FMB NPs, Ⅳ: FMB NPs + Laser, Ⅴ: FMBI NPs, Ⅵ: FMBI NPs + Laser, scale bar = 50 μm.)

References

(1) Tang, M.; Ni, J.; Yue, Z.; Sun, T.; Chen, C.; Ma, X.; Wang, L. Polyoxometalate-Nanozyme-Integrated Nanomotors (POMotors) for Self-Propulsion-Promoted Synergistic Photothermal-Catalytic Tumor Therapy. *Angew. Chem. Int. Edit.* **2024,** *63* (6), e202315031.